Research papers

Importance of infragravity waves in a wave-dominated inlet under storm conditions

Diogo Mendes [a,b,c,*], André B. Fortunato [b], Xavier Bertin [d], Kévin Martins [e,d], Laura Lavaud [d], Ana Nobre Silva [f], António A. Pires-Silva [a], Thibault Coulombier [d], José P. Pinto [c]

[a] CERIS, Instituto Superior Técnico, Universidade de Lisboa, Lisbon, Portugal
[b] National Laboratory for Civil Engineering, Lisbon, Portugal
[c] Hydrographic Institute, Lisbon, Portugal
[d] UMR 7266 LIENSs CNRS-Université de La Rochelle, Institut Du Littoral et de L'Environnement, La Rochelle, France
[e] UMR 5805 EPOC CNRS-Université de Bordeaux, Bordeaux, France
[f] IDL, Faculdade de Ciências, Universidade de Lisboa, Lisbon, Portugal

ARTICLE INFO

ABSTRACT

The processes associated with infragravity waves (IGW) and their role on the hydro-sedimentary dynamics of a wave-dominated inlet are investigated using field observations collected at the Albufeira Lagoon (Portugal) during storm Leslie in October 2018. During the storm, significant IGW heights reached up to 1.0 m in the surf zone and 0.4 m inside the lagoon. IGW frequencies were blocked by ebb currents at the flood-delta and this effect was stronger for higher IGW frequencies. Therefore, low-frequency IGW were able to propagate further into the inner lagoon. The application of a 1D energy balance equation suggests that depth-induced breaking and bottom friction contributed equally to dissipate IGW energy at the flood-delta and that this dissipation was stronger during the flood than during the ebb.

Large horizontal velocities under IGW crests increased the instantaneous suspended sediment transport rate by up to two orders of magnitude during flood at the flood-delta. The net suspended sediment transport rate and its variability, associated with the wave motion, was positive (landward) during flood and negligible during ebb. These positive values were associated with large wave-induced orbital velocities, suggesting that waves were more effective than tidal currents in inducing suspended sediment transport. The oscillatory suspended sediment transport rate was directed towards the lagoon and dominated by IGW frequencies. The observed sediment accretion of the northern channel occurred during the most energetic IGW. The measurements presented in this study and their analyses demonstrate how IGW play a major role in the sedimentary dynamics of wave-dominated inlets during storm conditions.

1. Introduction

Coastal lagoons are water bodies commonly found along sandy coastlines and they are connected to the open sea through tidal inlets. These aquatic systems are sheltered from wind-generated waves by sand spits and/or barrier islands and serve as habitat to many species. Many leisure and economic activities, such as water sports, navigation and fishing, take place inside coastal lagoons, reflecting their socio-economical interest (e.g. Newton et al., 2014).

Tidal inlets can be classified as tide-dominated, mixed energy or wave-dominated, based on the mean tidal range and the mean wave height (Hayes, 1979). The tidal prism, defined as the volume of water discharged through the tidal inlet during a flood or an ebb tide, partially controls the stability of a tidal inlet (Bruun, 1978). The stability of a tidal inlet can be defined as the ability to maintain its shape and position over time. Wave-dominated inlets are often unstable, because energetic offshore wave conditions are typically associated with morphological evolutions that occur at the time scale of days or weeks, and tend to close naturally (McSweeney et al., 2017). Understanding the exchanges of sediments through tidal inlets is important from a coastal management perspective.

The physical processes contributing to the seasonal morphological
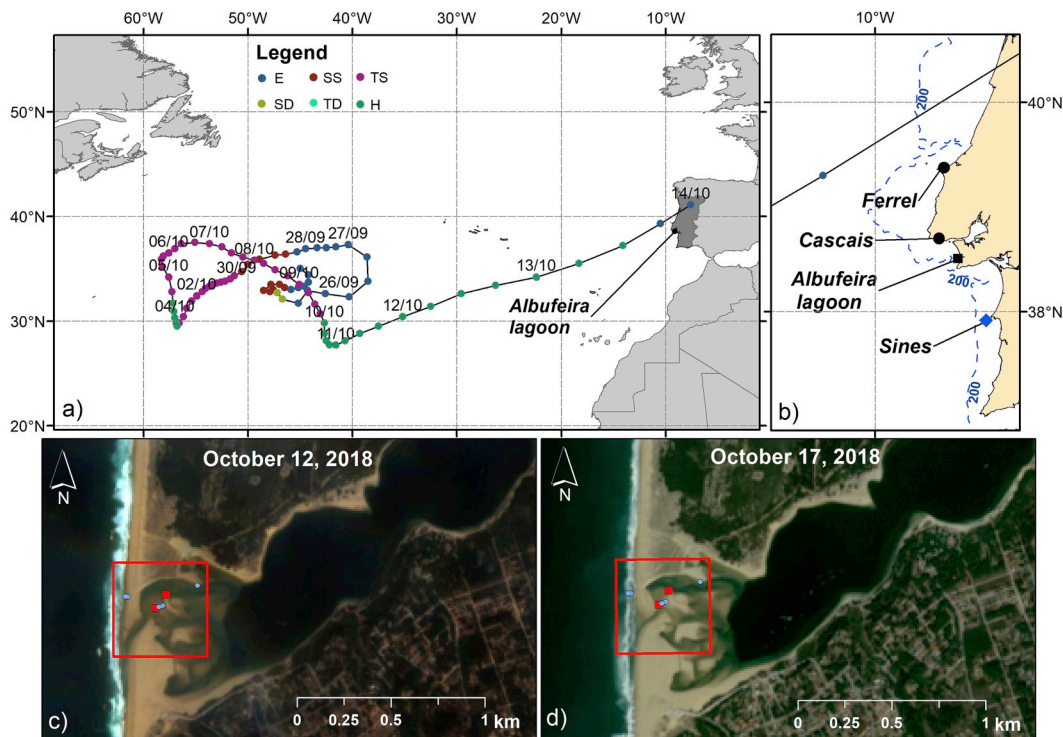

Fig. 1. (a) Leslie's track obtained from Pasch and Roberts (2019); (b) geographical location of the study site, extent of the continental shelf (blue dashed line) and place names: Albufeira lagoon (black square), Cascais tidal gauge and meteorological station (black dot), Ferrel meteorological station (black dot), Sines wave buoy (blue diamond) and Leslie's track (black line); (c) and (d) Satellite images from Sentinel-2 mission (Copernicus programme of European Space Agency - Drusch et al., 2012) with a spatial resolution of 10 m obtained before (c) and after (d) hurricane Leslie. The abbreviations in the legend stand for E – extratropical; SD – subtropical depression; SS – subtropical storm; TD – tropical depression; TS – tropical storm; H - hurricane. The red boxes indicate the spatial limits of Figs. 3 and 13, the red squares are the ADP locations and the light blue circles are the PT locations. (For interpretation of the references to colour in this figure legend, the reader is referred to the Web version of this article.)

evolution of a wave-dominated inlet were analysed by Bertin et al. (2009) combining field observations with a morphodynamic modelling system. These authors attributed the widening and deepening of the tidal inlet main channel observed during summer months to the ebb-dominance associated with tidal velocity asymmetry, usually under low wave energy conditions. In the winter months, these authors found that the wave-induced processes were responsible for the tidal inlet shoaling. In addition, the interaction between waves and tidal currents plays a major role in such shallow water systems (e.g. Olabarrieta et al., 2011; Dodet et al., 2013; Wargula et al., 2018). Wave-induced currents enhance the sediment transport during flood and reduce the tide-induced sediment transport during the ebb, thereby promoting flood-dominance at the tidal inlet. These findings were corroborated by field studies that investigated short wave-induced processes in wave-dominated inlets (e.g. Orescanin et al., 2014; Orescanin and Scooler, 2018; Wargula et al., 2014). State-of-art morphodynamic models are capable of reproducing the short-term morphological evolution of shallow inlets but they often fail to reproduce its closure (e.g. Dodet, 2013). This suggests that other physical processes not accounted for in such models might contribute to the closure of shallow inlets.

In addition to wind-generated short-waves (SW), with periods between 4 s and 25 s (0.04–0.25 Hz), the spectrum of ocean waves displays other types of oscillations such as infragravity waves (Munk, 1950). Infragravity waves (IGW) are low-frequency oscillations with periods between 25 s and 250 s (0.004–0.04 Hz) associated with and enhanced by the wave grouping of SW. Bertin et al. (2018) recently provided a thorough review on the generation and propagation of IGW and on their importance in several coastal environments. Although field observations of IGW have been reported for several decades (e.g. Tucker, 1950), the importance of IGW in wave-dominated inlets or in shallow and small estuaries has only been investigated recently (Williams and Stacey,

2016; Bertin and Olabarrieta, 2016).

Williams and Stacey (2016) analysed field observations collected in the Pescadero estuary (California) and identified low-frequency oscillations in water levels and horizontal velocities associated with the range of IGW frequencies. The significant IGW height inside the estuary increased with more energetic offshore wave conditions, in agreement with previous observations (e.g. Wright et al., 1982). Moreover, IGW orbital velocities were stronger on flood than on ebb. Williams and Stacey (2016) attributed this behaviour to the hydraulic disconnection between the estuary and the ocean that occurs around low-tide.

Bertin and Olabarrieta (2016) investigated the IGW generation and propagation combining field observations with the application of the XBeach model (Roelvink et al., 2009) at the Albufeira Lagoon (Portugal). IGW and associated orbital velocities were stronger on flood than on ebb at this lagoon. The authors showed that IGW decreased due to the interaction with opposing tidal currents. In this lagoon, IGW are blocked because the magnitude of ebb currents can reach the IGW group velocity at the inlet channel. Additionally, Bertin and Olabarrieta (2016) proposed that the peaks in currents associated with IGW during flood can promote flood-dominance, potentially contributing to the closure of the inlet.

The closure of shallow, wave-dominated inlets is generally associated with storm conditions, which drive larger morphological changes compared to situations with mild wave conditions. Large IGW waves (>1 m) are also expected to develop under storm conditions on beaches (e.g. De Bakker et al., 2014; Fiedler et al., 2015; Inch et al., 2017; Wright et al., 1982). While the role of large IGW during storm conditions has been investigated on dune morphodynamics (e.g. McCall et al., 2010), the role of large IGW in wave-dominated inlets is limited to a few studies. This study investigates IGW-induced processes and their role on the hydro-sedimentary dynamics of a wave-dominated inlet during a

storm. The study is based on the analysis of field observations collected at the Albufeira Lagoon (October 12–15, 2018) during the passage of the hurricane Leslie. Bertin et al. (2019) used a subset of this dataset to discuss the hypothesis that IGW can trigger the closure of wave-dominated inlets. The present study uses the dataset to perform a more comprehensive analysis.

This paper is organized as follows. The field experiment is described in section 2, which specifies the environmental conditions, the deployment of the instruments and the topographic surveys. Section 3 describes the methods used to analyse the field data. Section 4 investigates the IGW-induced processes from a hydrodynamic perspective, namely the propagation of IGW from the surf zone to the flood-delta and to the inner lagoon, the physical processes that contribute to IGW reduction and dissipation at the flood-delta and the relative importance of IGW and SW orbital velocities. Section 5 examines the inlet's sedimentary dynamics, in particular the contribution of IGW to the suspended sediment transport rate at the flood-delta and the inlet short-term morphological evolution during hurricane Leslie. The conclusions are summarized in section 6.

2. Study site and field experiment

2.1. Albufeira lagoon

The Albufeira lagoon, located on the Western Portuguese Coast, is connected to the Atlantic Ocean by a typically narrow (<50 m) and shallow (<2 m) inlet channel (Fig. 1c and d). This lagoon is located on the Caparica-Espichel littoral arc, fronted by a continental shelf with variable width, ranging from 5 km West of the Albufeira lagoon to about 40 km West of the Tagus estuary (Fig. 1b). The Albufeira lagoon has a river basin area of 100 km^2, a lagoon area of 1.6 km^2 and a negligible river discharge when compared to its tidal prism (Freitas, 1995). The oceanic semidiurnal tidal range in front of the Albufeira lagoon varies between 0.55 m and 3.86 m (Guerreiro et al., 2015). The offshore wave regime is energetic with an average deep-water winter (summer) significant wave height of 2.65 m (1.57 m) (Dodet et al., 2010). Following Hayes's diagram, this ephemeral inlet can be classified as wave-dominated. The inlet is artificially opened in April during spring tides to promote water renewal and usually closes during the maritime winter under storm waves (Fortunato et al., 2014; Moreira et al., 2019). Bottom sediments are typically coarse with a median sediment diameter of 0.9 mm based on a grain-size analysis performed on sediment samples collected at the flood-delta. The steep adjacent beaches exhibit a bottom slope of up to 1/10 and can thus be characterized as reflective following the classification of Wright and Short (1984).

2.2. Meteo-oceanographic conditions

During the observational period between October 12 and 15, the Portuguese coastline was hit by the hurricane Leslie (Pasch and Roberts, 2019). Leslie was formed in the centre of the North Atlantic Ocean on September 23 and moved to the northeast near the study site (Fig. 1a and b). The former hurricane transitioned to an extratropical cyclone (hereafter storm Leslie) about 500 km from the Portuguese coastline. Landfall occurred on October 14 about 200 km north of the study site. Near landfall, the maximum wind gusts associated with the Leslie storm reached up to 170 km/h. These winds left 300,000 homes without electricity, uprooted 1000 trees and caused 1900 incidents. The Portuguese Insurance Agency (Associação Portuguesa de Seguradores - APS) reported 28,000 occurrences with an estimated damage cost of 70 million euros (APS, 2018).

The significant wave height at the Sines buoy during winter storms can be higher than that during storm Leslie. The significant wave height associated with a 2-year (10-year) return period is 8.2 m (10.4 m) (Fortunato et al., 2017). Quadrio and Taborda. (2009) analysed the annual and quasi-decadal storminess along the western Portuguese
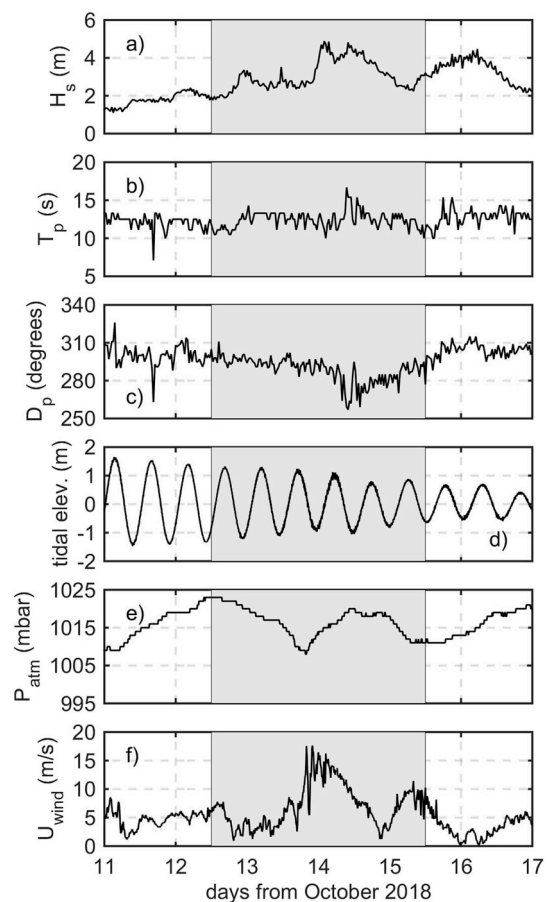

Fig. 2. Time-series of: (a) significant wave height (H_s) measured by Sines wave buoy; (b) peak wave period (T_p) measured by Sines wave buoy; (c) mean peak wave direction (D_p) measured by Sines wave buoy; (d) tidal elevation measured by the Cascais tidal gauge referred to mean sea level; (e) atmospheric pressure at mean sea level (P_{atm}) measured by the Cascais meteorological station; (f) mean wind velocity (U_{wind}) measured by the Ferrel meteorological station. The grey area represents the time period when the instruments were deployed at the Albufeira lagoon.

coastline. A storm event was defined with a significant wave height larger than 5 m and with a minimum time interval of 12 h between events. Based on an analysis of Sines buoy measurements between 1986 and 1993, these authors reported an average of 9.3 stormy days per year. Yet, these stormy days are most likely to occur during the maritime winter (Moreira et al., 2019) when the Albufeira lagoon inlet is usually closed. Storm Leslie was responsible for the morphological evolutions that occurred at the Albufeira lagoon which were particularly noticeable at the northern sand spit close to the inlet channel (Fig. 1c and d).

Meteo-oceanographic conditions used in this study were recorded at four locations, namely at the Sines wave buoy moored at 100 m water depth, at the Cascais tidal gauge, at the Cascais meteorological station and at the Ferrel meteorological station (Fig. 1b). During the passage of Leslie, between October 13 and 15, the maximum value of the significant wave height registered by the Sines buoy was 4.8 m (Fig. 2a), the peak wave period reached 16 s (Fig. 2b) and the mean peak wave direction rotated from north-west to west-southwest (Fig. 2c). The measured tidal range at Cascais decreased from 2.6 m on October 12 to 1.2 m on October 16 (Fig. 2d). Consequently, the field experiment took place during the transition from spring to neap tides. The atmospheric pressure at Cascais decreased by 15 mbar during the passage of Leslie (Fig. 2e) and the 10-min averaged wind velocity at Ferrel displayed a maximum value of 18 m/s (Fig. 2f).
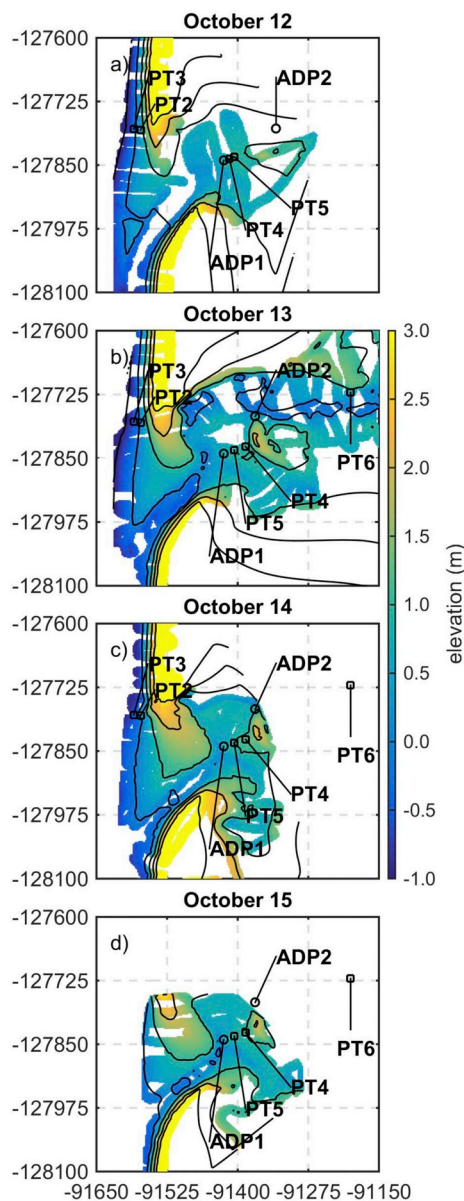
Fig. 3. Topographic survey performed on: (a) 12 October 2018; (b) 13 October 2018; (c) 14 October 2018; (d) 15 October 2018. Spatial locations of acoustic Doppler current profilers (circles) and pressure transducers (squares). Elevation is referred to mean sea level at Cascais tidal gauge (2.08 m above the nautical chart datum) and the horizontal coordinates are referred in the ETRS89 PT-TM06 system. Blank areas constitute nodes of the digital elevation model (DEM) grid that have a distance higher than 10 m than any RTK-DGPS measured point. (For interpretation of the references to colour in this figure legend, the reader is referred to the Web version of this article.)

2.3. Description of the topographic surveys

A topographic survey of the inlet near the transitional channel was performed at every low-tide during daylight hours between 12 and 15 October 2018 (Fig. 3). The topographic surveys were conducted using two RTK DGPS (mounted on a backpack). Tidal asymmetry at the Albufeira lagoon induced by the inlet is associated with a 2-h phase lag between the low tides in the ocean and in the lagoon. Therefore, the topographic survey started at the adjacent beaches during low-tide and progressed landward. A digital elevation model (DEM) was generated for each daily topographic survey using a natural neighbour interpolation method with a regular grid spacing of 2 m. Only DEM grid nodes within a Euclidean distance smaller than 10 m from any RTK DGPS

Table 1
Instrument deployment. Horizontal coordinates (X, Y) are referred in the ETRS89 PT-TM06 system. Elevation (Z) is referred to mean sea level at Cascais tidal gauge (2.08 m above the nautical chart datum). z_0 is the distance between the instrument and the bottom during deployment. Parenthesis indicate the values for instruments that were re-deployed.

Instrument	X (m)	Y (m)	Z (m)	z_0 (m)
PT2	−91571.86	−127780.74	0.54	0.00
			(0.18)	
PT3	−91584.13	−127779.31	−0.21	0.00
			(−0.42)	
ADP1	−91424.62	−127841.40	0.91	0.15
PT4	−91414.55	−127837.70	0.93	0.00
	(−91386.14)	(−127827.14)	(1.02)	
PT5	−91405.90	−127834.46	1.00	0.00
ADP2	−91331.53	−127777.9	0.89	0.20
	(−91369.41)	(−127767.94)	(1.22)	(0.20)
PT6	−91199.87	−127721.03	0.70	0.10

measured point were considered (Fig. 3). The lack of topographic measurements in the transitional channel on October 12 and 14 is due to the strong tidal currents that prevented a safe survey work.

2.4. Instrumentation and data acquisition

During the field experiment, several instruments were deployed at the Albufeira lagoon (Fig. 3). An acoustic Doppler current profiler (ADP1) co-located and synchronized with a pressure transducer (PT) and an optical backscatter sensor (OBS) was deployed at the flood-delta. A second similar acoustic Doppler current profiler (ADP2) co-located and synchronized with a PT and an OBS was deployed near the northern channel. Two pressure transducers (PT3 and PT2) were deployed at the adjacent beach. Two pressure transducers (PT4 and PT5) were deployed near ADP1 at the flood-delta and a pressure transducer (PT6) was deployed in the inner lagoon.

The PT2-5 were placed just below the bottom (~0.05 m) inside stainless steel tubes that were buried in the bed. The ADP1 was deployed on a large stainless steel screw structure 0.15 m above the bottom and the co-located OBS was installed 0.10 m above the ADP pressure sensor, at the location of the first measuring cell. The ADP2 was deployed on a scaffold stainless steel frame 0.20 m above the bottom with a co-located OBS installed in the same way as for ADP1. The PT6 was attached to a stainless steel tube located in the inner lagoon and placed 0.10 m above the bottom.

ADP1-2 and PT2-5 were deployed during the low-tide on October 12. On October 13, the PT6 was deployed and the locations of PT4 and ADP2 were slightly adjusted. The PT2-3 and the PT6 were retrieved on October 14 and 16, respectively, and the remaining instruments were recovered on October 15. Data obtained by PT4 and by ADP2 before the re-deployment (October 13) were not used in the following analyses. Table 1 summarizes the information on the instrumentation deployment.

The PT2-5 were configured to acquire pressure data in a continuous mode with a sampling frequency of 4 Hz and a resampling to 2 Hz was performed to account for small (<1 s) time drifts. The PT6 acquired pressure data continuously with a sampling frequency of 2 Hz. Each ADP was configured to record high-sampling and time-averaged measurements every 30 min. Both ADPs were set to measure velocities in an East-North-Up coordinate system. Measurements of near-bottom pressure, horizontal velocities and sediment concentration were obtained with bursts of 20 min every 30 min with a sampling frequency of 2 Hz. Pressure measurements at ADP1 (ADP2) were registered 0.15 m (0.20 m) above the bed, horizontal velocities were recorded in a near-bottom cell 0.50 m thick and sediment concentrations were obtained 0.10 m above the pressure measurements at each ADP. The sediment concentrations were obtained after laboratory calibration using sediment samples collected at each ADP location. A recirculation tank was used to

Table 2
Main flow orientation (θ) at ADP1 obtained with a Principal Component Analysis.

Tidal cycle	θ (degrees) to North
1	40.7
2	43.4
3	36.5
4	32.8
5	14.7
6	−3.0

calibrate sediment concentrations up to 23 kg/m^3. The correlation co-efficient (R^2) value associated with the linear calibration equation was 0.93 (0.95) for the OBS at the ADP1 (ADP2) location. The blanking distance and the cell size of each ADP was 0.10 m.

3. Data analysis

3.1. Data preparation

The full time-series of raw pressure records obtained by the PT2-6 were corrected using the sea level atmospheric pressure at Cascais (Fig. 2e) and the distance between the pressure sensor and the bed (z_0). The full time-series were divided into blocks of 30 min and blocks that showed intermittently dry conditions were discarded, thereby excluding swash oscillations. For each block, the mean water depth (d) was equal to the time-averaged value of the water depth (h) by assuming a hydrostatic approximation. The sea-surface elevation (η) was obtained as

the difference between h and d. The procedure outlined above was the same for each ADP raw-pressure record but 20 min blocks were used instead. For the ADPs, only blocks with $d > 0.6$ m were used in the following analyses.

A 3rd order low-pass Butterworth filter, without phase lag and with a cut-off frequency (0.5 Hz) close to the Nyquist frequency, was used on the raw horizontal velocities (u,v) to remove possible noise. For each block, the mean horizontal velocities ($\overline{uv}$) were computed as the time-averages of the horizontal velocities (u,v). The oscillatory horizontal velocities (u_{osc}, v_{osc}) were obtained as the difference between ($\overline{uv}$) and (u, v). The main flow direction (θ) at the ADP1 location was determined for each tidal cycle using a Principal Component Analysis (PCA) using $\overline{u}$ and $\overline{v}$ as inputs. θ was used to rotate u and v for each tidal cycle (Table 2). Henceforth, u and v will denote velocities along θ and perpendicular to θ, respectively. The analyses will mostly focus on u since it is usually much larger than v. While the flood and ebb currents display opposite directions at ADP1, currents at ADP2 are generally directed to the North-East during the flood and to the West (along with the northern channel) during the ebb due to the surrounding topography (Fig. 3). Hence, instead of the PCA we used an angle of 50° to North to rotate u and v at ADP2. The angle of 50° to North is approximately the main flow direction at ADP2 during the flood when the larger mean velocities were measured (October 14).

The suspended sediment concentration (c) values higher than the calibrated range (23 kg/m^3) were extrapolated, as in De Bakker et al. (2016), using the linear calibration equations. Negative values of c were set to zero. For each 20 min block, a de-spiking procedure was performed on the c time-series as in Storlazzi and Jaffe (2002) in order to
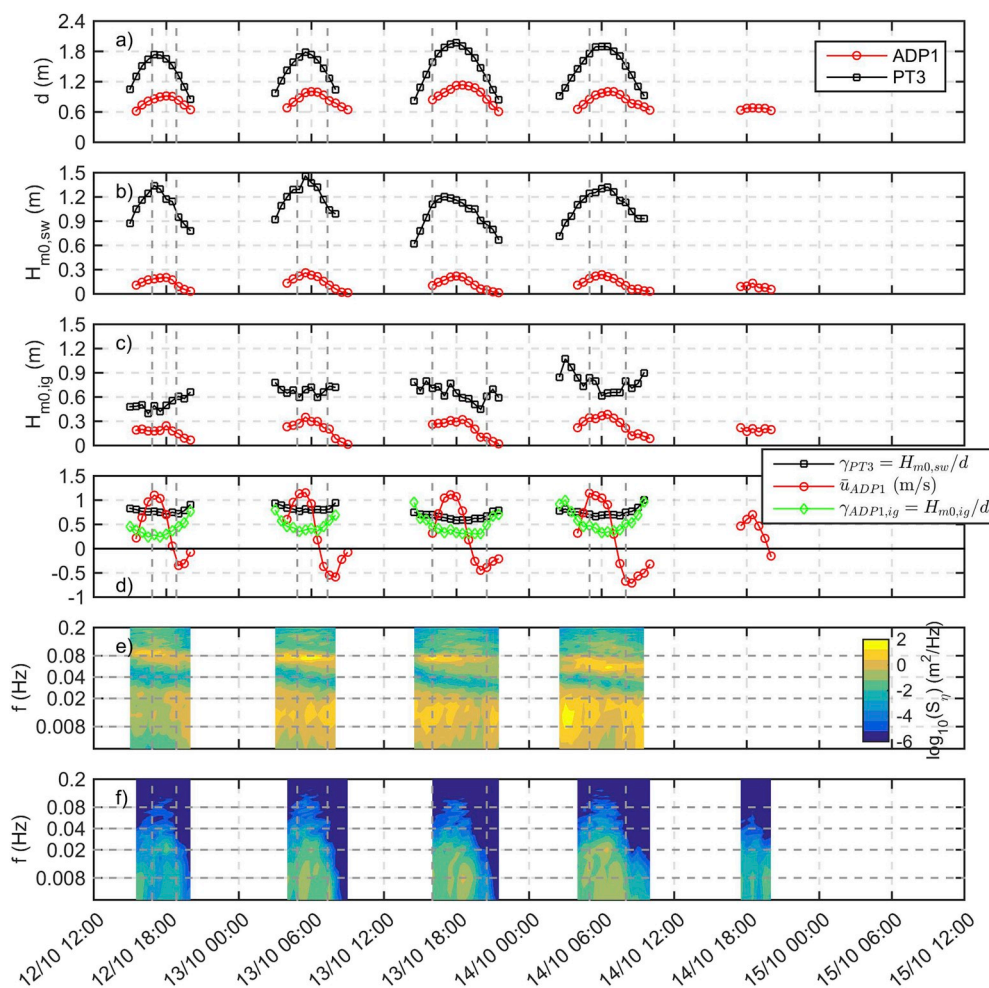

Fig. 4. Time-series of: (a) mean water depth (d); (b) significant short-wave height ($H_{m0,sw}$); (c) significant infragravity height ($H_{m0,ig}$); (d) relative short-wave height (γ_{PT3}) at the PT3 location, time-averaged velocity ($\overline{u}$) at the ADP1 location and relative infragravity wave height ($\gamma_{ADP1,ig}$) at the ADP1 location; (e) spectrogram of sea-surface elevation variance density at the PT3 location; (f) spectrogram of sea-surface elevation variance density at the ADP1 location. Vertical dashed lines indicate a similar water depth at flood and ebb at the ADP1 location. (For interpretation of the references to colour in this figure legend, the reader is referred to the Web version of this article.)

eliminate values associated with air bubbles. Values of $c(t) > \bar{c} + 3\sigma_c$ were removed and re-interpolated using a cubic spline. $\bar{c}$ and σ_c are the time-averaged and the standard deviation of c, respectively, for each block. The replaced values always represented less than 2% of the number of values in each block.

3.2. Bulk short wave and infragravity wave parameters

A variance spectral density wave spectrum (S_η) was calculated with the Welch's method (Welch, 1967) using η as input for each block. Hanning-windowed sub-samples of 512 points were 50% overlapped which resulted in a spectrum with a frequency resolution (df) of 0.0039 Hz and with 16 and 26 degrees of freedom (dof) for the ADP and the PT data, respectively. Different dof were used to maintain the same df among instruments.

Estimating η associated with the wave motion using a pressure sensor near the bottom usually requires a correction factor (K). K is often based on linear wave theory to take into account the wave-induced pressure attenuation over the water depth (Dean and Dalrymple, 1992). The interaction between waves and currents at tidal inlets may affect K. In this case, currents should be included in K through the Doppler effect (K_U) (e.g. Smith, 2002). At the ADP1 location, the use of K or K_U showed negligible differences (<0.01 m) when compared without K in terms of significant wave heights (not shown). Therefore, no correction factor was applied on S_η.

The nth order spectral moment (m_n) was obtained by integrating S_η:

$$m_n = \int_{f_{min}}^{f_{max}} S_\eta f^n df \tag{1}$$

where (f_{min}, f_{max}) were set to (0.0039, 0.04) Hz and to (0.04, 0.5) Hz for the IGW and SW frequency bands, respectively. The separation frequency of 0.04 Hz was chosen to approximately follow a spectral energy density valley between SW and IGW frequencies of S_η time-series obtained at the adjacent beach (see below – Fig. 4e). Some authors set the separation frequency to half of the offshore peak SW frequency (e.g. Rijnsdorp et al., 2015; Guérin et al., 2018). The values of half the peak SW frequency obtained using records at the Sines buoy (Fig. 2b) ranged between 0.04 Hz and 0.05 Hz during the field experiment, thus being close to the chosen 0.04 Hz separation frequency value. The significant wave height was obtained as:

$$H_{m0} = 4\sqrt{m_0} \tag{2}$$

Two significant wave heights were defined, namely the significant short-wave height ($H_{m0,sw}$) and the significant infragravity wave height ($H_{m0,ig}$). These two variables were obtained using (1) and the corresponding integration limits. The mean infragravity wave period ($T_{m02,ig}$) was obtained as $T_{m02,ig} = (m_{0,ig}/m_{2,ig})^{0.5}$ as an analogy with the mean SW period ($T_{m02,sw}$) (e.g. Holthuijsen, 2007).

3.3. Wave-generated orbital velocities

The wave-generated orbital velocity (u_{orb}) was calculated following Wiberg and Sherwood (2008) as

$$u_{orb} = \sqrt{2 \int_{f_{min}}^{f_{max}} S_u + S_v df} \tag{3}$$

where S_u and S_v are the horizontal velocity (u_{osc} and v_{osc}) spectra and (f_{min}, f_{max}) was set to (0.0039, 0.2) Hz. The IGW ($u_{orb,ig}$) and SW ($u_{orb,sw}$) orbital velocities were calculated by setting (f_{min}, f_{max}) to (0.0039, 0.04) Hz and to (0.04, 0.2) Hz, respectively. A value of $f_{max} = 0.2$ Hz was chosen because the comparison between the values of u_{orb} using (3) against the values of u_{orb} using linear wave theory can differ by up to a factor of 2 for $f_{max} > 0.2$ Hz likely due to noise associated with velocity measurements.

3.4. Suspended sediment transport rate

The net time-averaged suspended sediment transport rate (q_{net}) at a fixed distance from the bottom can be defined as

$$q_{net} = \overline{uc} \tag{4}$$

where the overbar denotes the average over 20 min. The variability in $q = uc$ was assessed through the calculation of the 10% and 90% per-centiles of q for each block. This variability is associated with the wave-induced sediment transport. The first tidal cycle at the ADP1 location was not considered in the following analysis because the correlation between the time-series of u and c was weak (<0.3).

The oscillatory suspended sediment transport rate (q_{osc}) was calculated to quantify the relative importance between IGW and SW for the wave-induced sediment transport as in Osborne and Greenwood (1992):

$$q_{osc} = \int_{f_{min}}^{f_{max}} R(CS_{u_{osc}c_{osc}}) df \tag{5}$$

where R is the real part of the co-spectrum (CS) between u_{osc} and c_{osc}, (f_{min}, f_{max}) was set to (0.0039, 0.2) Hz and c_{osc} is the difference between $\bar{c}$ and c. The IGW (q_{ig}) and SW (q_{sw}) suspended sediment transport rates were calculated by setting (f_{min}, f_{max}) to (0.0039, 0.04) Hz and to (0.04, 0.2) Hz, respectively.

4. Hydrodynamics

4.1. Propagation of short and infragravity waves through the inlet channel

At the PT3 location, the mean water depth is symmetric between flood and ebb due to the oceanic tide (Fig. 4a). The values of $H_{m0,sw}$ at that location are controlled by the water depth (Fig. 4b) with a relative wave height ($\gamma_{PT3} = H_{m0,sw}/d$) that ranges between 0.6 and 0.8 for $d > 0.8$ m (Fig. 4d). Therefore, PT3 was always located within the surf zone. For very shallow water depths ($d < 0.8$ m), γ increases to values above 0.8 (Fig. 4d). In the inner surf zone, waves become asymmetric and take a bore-like shape, characterized by steep wave fronts (Martins et al., 2018). The γ values associated with bores close to the shoreline can equal or even exceed unity (e.g. Nielsen, 2009; Power et al., 2010). Also, the interaction between an incident and a reflected wave may lead to a standing wave pattern which can increase the γ values (Martins et al., 2017). Similarly, the values of γ may also vary when IGW amplitudes become comparable to the water depth (Roelvink, 1993).

Unlike $H_{m0,sw}$, the values of $H_{m0,ig}$ at PT3 increase between the first and the fourth tidal cycle for similar d (Fig. 4c). This behaviour was attributed to the variation in offshore wave conditions experienced during the field campaign, ranging from moderate to energetic (Fig. 2a). Moreover, the values of $H_{m0,ig}$ at PT3 are similar between ebb and flood for each tidal cycle but, in general, slightly decrease around high-tide (Fig. 4c). This behaviour can be associated with IGW shoaling which would induce a variation of $H_{m0,ig}$ due to modifications in d.

As the tide propagates into coastal lagoons, it is damped and distorted by the narrow inlet and the shallow water depths (e.g. Keulegan, 1967; Speer and Aubrey, 1985; Bertin et al., 2009). The tidal distortion results in a larger phase lag at low tide than at high tide. At the flood-delta (ADP1), high-tide occurs in general 2 h later than at the adjacent beach (PT3) (Fig. 4a). The values of $H_{m0,sw}$ are reduced by about 90% between the surf zone (PT3) and the flood-delta (ADP1) (Fig. 4b). This reduction of $H_{m0,sw}$ can result from the SW dissipation due to depth-induced breaking at the ebb-delta and at the northern sand spit (Fig. 3) and also from SW refraction and diffraction near the inlet channel. Additionally, the values of $H_{m0,sw}$ at ADP1 are larger during the flood than during the ebb for similar water depths (Fig. 4b). This behaviour is explained by the interaction with ebb currents following Dodet et al. (2013) and Bertin and Olabarrieta (2016). Soon after slack tide, ebb currents increase the SW steepness which leads to wave energy
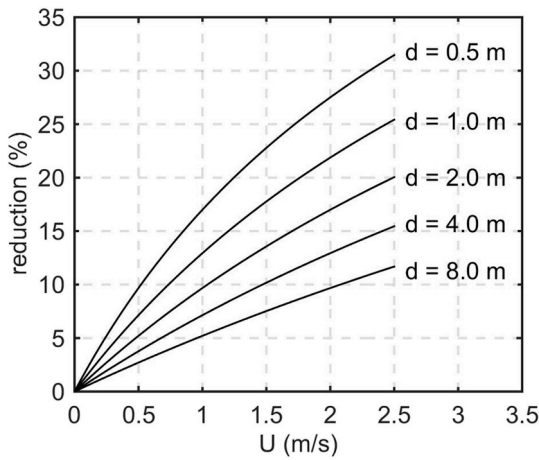
Fig. 5. Reduction (%) of infragravity wave energy as a function of a depth-integrated following current velocity (U) for different water depths (d).

dissipation by white-capping on the higher-frequencies of the SW frequency band (Fig. 5f). As the magnitude of the ebb current increases and matches the SW group velocity, full wave blocking occurs.

The values of $H_{m0,ig}$ were larger at the PT3 than at the ADP1 locations (Fig. 4c). Part of the IGW energy at PT3 is associated to IGW reflection at the steep beach. The IGW reflection coefficient at the PT3 location was inferred using the parameter (β_H) proposed by van Dongeren et al. (2007):

$$\beta_H = \frac{\alpha T_{m02,ig}}{2\pi} \sqrt{\frac{g}{H_{m0,ig}}} \qquad (6)$$

where the beach slope α is taken as 1/10. van Dongeren et al. (2007) verified that the IGW reflection coefficient is equal to 1 if $\beta_H > 1.25$ using laboratory measurements. At the PT3, the average value of β_H was 3.8 with a standard deviation of 0.4 over the field experiment. The IGW reflection coefficient is therefore equal to 1 which suggests that 50% of the IGW energy at the PT3 location originates from the full reflection of IGW at the shoreline. Considering this, the IGW energy flux at the ADP1 location is found to be approximately 30% (15%) during flood (ebb) of the incident IGW energy flux at the PT3 location. The minimum reduction of incident IGW energy flux between the two locations coincides with high tides, with for instance 50% reduction found on the 14/10 at 6AM. This highlights the importance of water depth at the inlet transitional channel and in the lagoon on the physical processes responsible for IGW energy changes. Refraction and diffraction of IGW spread laterally the amount of IGW energy after the inlet channel and can contribute to the reduction of $H_{m0,ig}$ between the surf zone (PT3) and the flood-delta (ADP1). Similar to $H_{m0,sw}$, the values of $H_{m0,ig}$ at ADP1 are larger during flood than during ebb (Fig. 4c). These differences are a result of the wave blocking due to ebb currents (Bertin and Olabarrieta, 2016). Moreover, the maximum values of $H_{m0,ig}$ occur later in time than the maximum values of $H_{m0,sw}$ (Fig. 4b and c). Bertin and Olabarrieta (2016) showed analytically that lower frequencies require higher counter-currents or smaller water depths to be blocked. Hence, higher frequencies are blocked earlier than lower frequencies (Fig. 4f). During flood, tidal currents can also affect $H_{m0,ig}$ at ADP1 due to an increase of the wave celerity. To demonstrate the role of flood currents on the changes in wave height (H), we consider the depth-integrated cross-shore energy flux balance based on linear wave theory in shallow waters neglecting alongshore variations and any dissipation between two locations (A and B). Moreover, we consider the effect of a possible
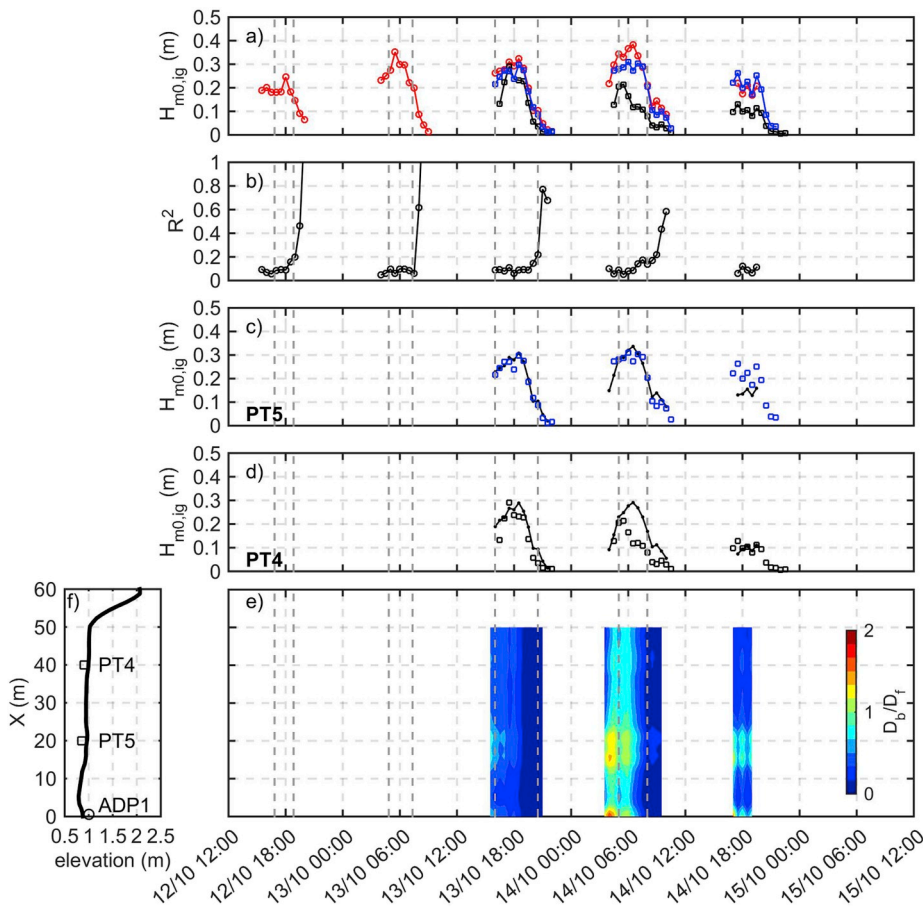

Fig. 6. Time-series of: (a) measured significant infragravity wave height ($H_{m0,ig}$) at the ADP1 (red circles), PT5 (blue squares) and PT4 (black squares) locations; (b) frequency-integrated infragravity wave reflection coefficient (R^2) computed following Sheremet et al. (2002) at the ADP1 location; (c) measured (squares) and calculated (black line) $H_{m0,ig}$ with the 1D energy flux balance equation at the PT5 location; (d) measured (squares) and calculated (black line) $H_{m0,ig}$ with the 1D energy flux balance equation at the PT4 location; (e) cross-shore variation of the ratio between infragravity wave dissipation by depth-induced breaking (D_b) and bottom friction (D_f). Topographic cross-shore transect with instrument locations (f). Vertical dashed lines indicate a similar water depth at flood and ebb at the ADP1 location. (For interpretation of the references to colour in this figure legend, the reader is referred to the Web version of this article.)
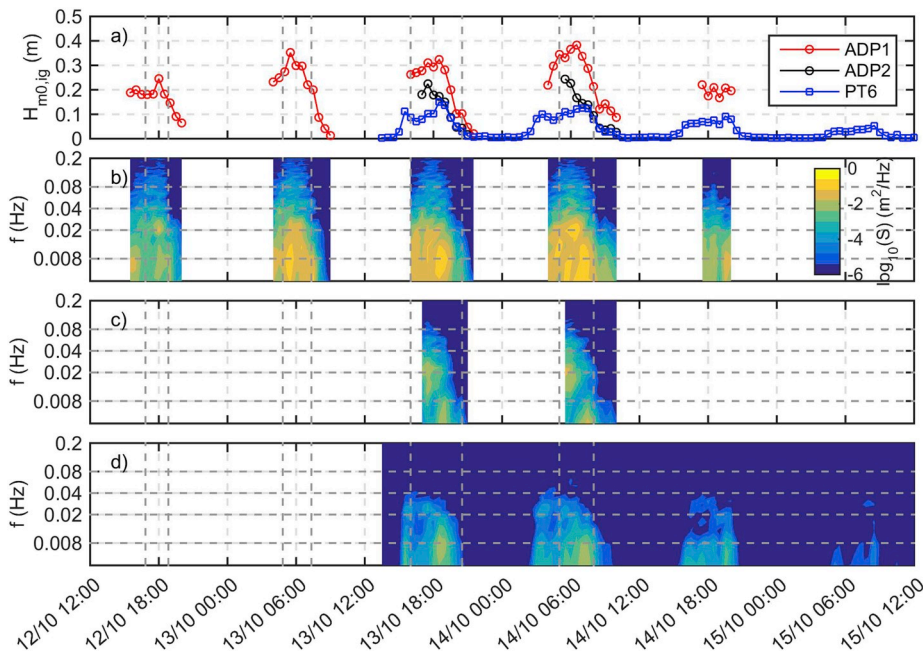
Fig. 7. Time-series of (a) significant infragravity wave height ($H_{m0,ig}$) at the ADP1 (red circles), at the ADP2 (black circles) and at the PT6 (blue squares) locations; (b) spectrogram of sea-surface elevation variance density at the ADP1 location; (c) spectrogram of sea-surface elevation variance density at the ADP2 location; (d) spectrogram of sea-surface elevation variance density at the PT6 location. Vertical dashed lines indicate a similar water depth at flood and ebb at the ADP1 location. (For interpretation of the references to colour in this figure legend, the reader is referred to the Web version of this article.)

depth-integrated flood current ($U > 0$ m/s) to be negligible at location A but not at location B. Under these conditions,

$$\frac{1}{8}\rho g H_A^2 \sqrt{g d_A} = \frac{1}{8}\rho g H_B^2 \left(\sqrt{g d_B} + U\right) \tag{7}$$

If we further consider that $d = d_A = d_B$ then,

$$\left(\frac{H_A}{H_B}\right)^2 = 1 + \frac{U}{\sqrt{gd}} \tag{8}$$

For a situation in which $d = 1$ m and $U = 1$ m/s, the ratio H_A/H_B is 1.15. This corresponds to a reduction of approximately 13% of H from A to B due to the flood current. The reduction of H as a function of U and d shows the importance of this effect in mixed-energy and tidal dominated inlets that are characterized by larger water depths at the transitional channel (Fig. 5). As d increases, the reduction decreases logarithmically for the same U. Therefore, this reduction is more important for shallow wave-dominated inlets than for other types of inlets.

4.2. Reduction of infragravity wave energy between the inlet channel and the inner lagoon

The values of $H_{m0,ig}$ over the flood-delta decreased eastward, i.e., away from the inlet mouth (Fig. 6a). This decrease is particularly strong during the Leslie storm on October 14. Several studies associate IGW dissipation on sandy beaches to IGW depth-induced breaking (e.g. van Dongeren et al., 2007; De Bakker et al., 2014; Inch et al., 2017) and to bottom friction (e.g. Rijnsdorp et al., 2015). IGW energy losses can also occur due to nonlinear energy transfers from IGW to SW frequencies (e.g. Ruju et al., 2012; Guedes et al., 2013; Mendes et al., 2018). The physical processes responsible for the decrease of $H_{m0,ig}$ over the flood-delta were investigated through the application of a 1D energy flux balance equation (hereafter 1DEB), detailed in Appendix A, over a transect that includes the ADP1, the PT4 and the PT5. IGW dissipation by depth-induced breaking (D_b) and the IGW dissipation due to bottom friction (D_f) were incorporated in the 1DEB.

The time-series of $H_{m0,ig}$ obtained with the 1DEB was compared with the measured values of $H_{m0,ig}$ at the PT4 and PT5 locations (Fig. 6c and d). In general, the 1DEB is able to reproduce fairly well the variation of

$H_{m0,ig}$ between the ADP1 and the PT4 and PT5 locations. The largest differences occur soon after slack tide on October 14. Two sensitivity analyses were performed in order to reduce these differences. The γ_{1DEB} values associated with D_b were varied between 0.3 and 0.6 and the hydraulic roughness related to D_f was computed with a different formulation (Appendix A). The following analysis is based on results with $\gamma_{1DEB} = 0.4$ and using a hydraulic roughness in the computation of D_f that accounts for bed form dimensions using the formulation of Grant and Madsen (1982), with bedload sediment transport and with sand grains (Appendix A).

The relative importance of depth-induced breaking and bottom friction over the cross-shore transect was assessed by comparing the space-time variation of D_b/D_f (Fig. 6e). In general, D_b/D_f is largest during flood with values reaching up to 1.5 during storm Leslie (October 14). Based on this analysis, D_b and D_f contribute equally in general to explain the IGW dissipation (Fig. 6a) over the flood-delta transect and D_b is slightly larger than D_f on October 14 during the flood.

The differences between the results of 1DEB and the observed values at PT4 and at PT5 were investigated through the calculation of the frequency-integrated reflection coefficient (R^2) (Fig. 6b) using the method of Sheremet et al. (2002). Soon after high-tide, on October 14 at 08h00, the value of R^2 increases from 0.1 to 0.2. This increase is likely due to wave reflection at the steep margin of the sand bank ($X \sim 55$ m in Fig. 6f). Wave reflection is not taken into account in the 1DEB and might have contributed to the differences between the 1DEB computations and the observations. Note that the effects of wave refraction, wave diffraction and wave interaction with tidal currents between the inlet channel and the ADP1 location were taken into account because the boundary conditions were given by the measured values at the ADP1 location. The effects of wave refraction are presumably small over the transect due to the flatness of the bottom at the flood-delta (Fig. 3). The effects of wave diffraction between ADP1 and PT4 locations were calculated using the analytical equation of Penney and Price (1952) with an inlet channel width of 50 m and a mean water depth of 0.8 m. Wave diffraction reduces H by 6% for the $T_{m02,ig}$ at the PT3 and ADP1 locations (60 s) and is considered negligible.

Similar to the reduction of $H_{m0,ig}$ at the flood-delta, the values of $H_{m0,ig}$ decreased between the flood-delta (ADP1), the northern channel (ADP2) and the inner lagoon (PT6) (Fig. 7a). The general patterns observed in the spectrograms of the sea-surface elevation at the different
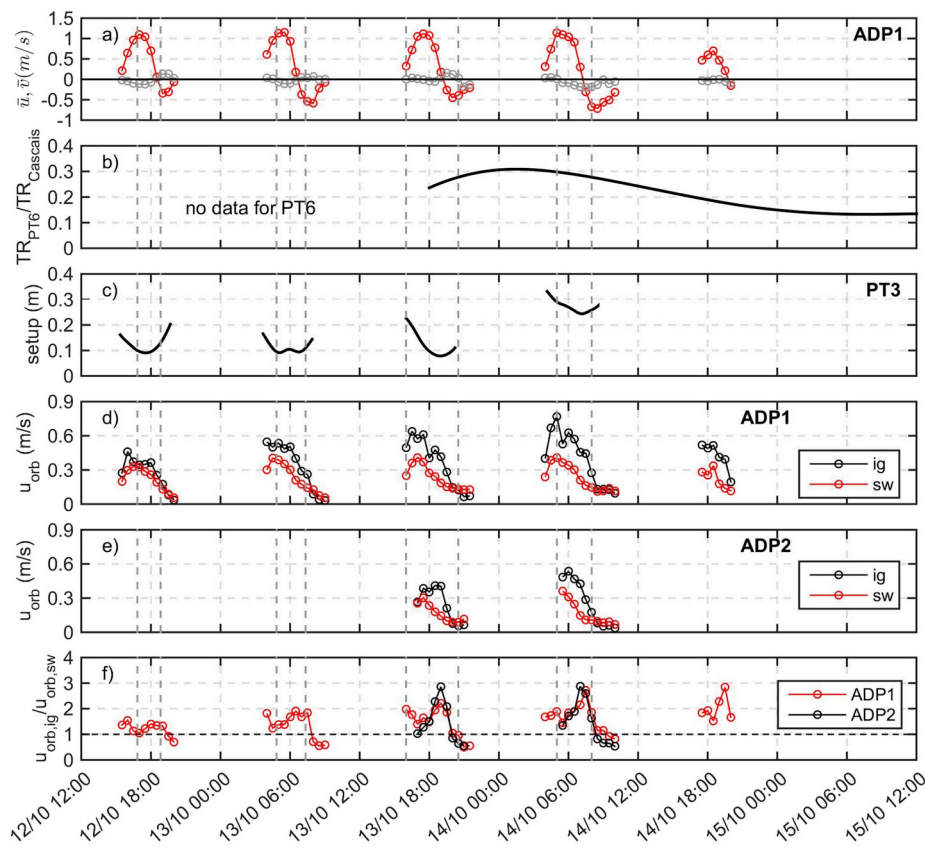
Fig. 8. Time-series of (a) the time-averaged velocity along the main flow direction ($\overline{u}$) (red circles) and perpendicular to it ($\overline{v}$) (grey circles); (b) the ratio between the tidal range at PT6 (TR_{PT6}) and at Cascais tidal gauge ($TR_{Cascais}$); (c) the wave setup at the PT3 location; (d) the wave-generated short-wave ($u_{orb,sw}$, red circles) and infragravity wave orbital velocities ($u_{orb,ig}$, black circles) at the ADP1 location; (e) the $u_{orb,sw}$ (red circles) and $u_{orb,ig}$ (black circles) at the ADP2 location; (f) the ratio $u_{orb,ig}/u_{orb,sw}$ at the ADP1 (red circles) and ADP2 (black circles) locations. Vertical dashed lines indicate a similar water depth at flood and ebb at the ADP1 location. (For interpretation of the references to colour in this figure legend, the reader is referred to the Web version of this article.)

locations (ADP1, ADP2 and PT6) (Fig. 7b–d) indicate that the spectral energy density is different between flood and ebb and between the high- and low-frequencies in the IGW frequency band. First, spectral energy density in the high-frequency part of the IGW frequency band (>0.008 Hz) is present at the ADP1 and ADP2 locations only during flood. Second, spectral energy density in the low-frequency part of the IGW frequency band (<0.008 Hz) is present at the ADP1, ADP2 and PT6 locations during almost the full tidal cycle. The absence of spectral energy density for $f > 0.008$ Hz during ebb at all locations can be attributed to ebb currents because these IGW frequencies require less intense currents to be blocked (Bertin and Olabarrieta, 2016). Additionally, IGW dissipation through depth-induced breaking is less intense for low- than for high-frequencies in the IGW frequency band (e.g. Battjes et al., 2004). The spectral energy density associated with $f < 0.008$ Hz is less prone to be blocked by ebb currents or to be dissipated by depth-induced breaking at the flood-delta. Consequently, low-frequency IGW are better able to propagate until ADP2 and PT6 locations. The effect of IGW refraction and diffraction can also play a role between ADP1 and ADP2 and PT6 locations to explain the variations of $H_{m0,ig}$ over the tidal cycle.

4.3. Tidal currents, infragravity and short-wave orbital velocities

The comparison between the first and last tidal cycles reveals a decrease in the maximum $\overline{u}$ at the ADP1 location from 1 m/s to 0.5 m/s (Fig. 8a). This decrease can be partly explained by a reduction of the offshore tidal amplitude because the field experiment took place between spring and neap tides (Fig. 2d). However, the decrease between the first and the last tidal cycles is not monotonic as would be expected due to the ocean conditions alone and the maximum $\overline{u}$ is approximately 1.2 m/s during the fourth tidal cycle (Fig. 8a). We investigated this observation by calculating the ratio between the tidal range at the PT6 location (TR_{PT6}) and at the Cascais tidal gauge ($TR_{Cascais}$). This ratio was calculated by adjusting a 3rd order spline to the maxima and minima of

the tidal level and it ranges from 0 to 1. Generally, and in wave-dominated inlets, values close to 1 would indicate a negligible influence of the inlet on the tidal range while values close to 0 would correspond to a closed inlet. During winter months, this ratio decreases due to inlet infilling induced by storms which promotes sediment accretion at the lagoon entrance (e.g. Oliveira et al., 2006; Bertin et al., 2009). During the field experiment, $TR_{PT6}/TR_{Cascais}$ increased during storm Leslie (October 14) and decreased later on (Fig. 8b). This behaviour indicates that the tidal amplitude increased inside the lagoon. The topographic surveys showed that there was an accretion of the inlet near the northern sand spit between October 13 and 14 (Fig. 3) which would reduce the tidal amplitude. We calculated the wave setup as the difference between the mean water depth at the PT3 location and at the Cascais tidal gauge (Fig. 8c) to understand if the tidal amplitude increase was due to an increase in mean sea level associated with the wave setup. Note that the wind-induced setup along the Portuguese coast is small because the continental shelf is narrow (Alvarez Fanjul et al., 1998). Moreover, a simple calculation of the wind-induced setup inside lagoon gives a value of 0.02 m which is smaller than the wave-induced setup (Fig. 8c). The maximum values of $TR_{PT6}/TR_{Cascais}$ on October 14 coincided with an increase of the maximum wave setup at the PT3 location from 0.20 to 0.30 m (Fig. 8b and c). Therefore, the increase of $TR_{PT6}/TR_{Cascais}$ on October 14 was due the wave setup, which reduced the tidal energy dissipation at the inlet. The tidal amplitude growth induced by the wave setup on October 14 increased the magnitude of flood currents (Fig. 8a–c). Previous studies on wave-dominated inlets highlighted the effect of the wave setup in increasing tidal amplitude inside lagoons (e.g. Bertin et al., 2009; Wargula et al., 2014). Here, we show that the increase of the mean sea level inside the lagoon due to the wave setup can also increase the tidal currents at the flood-delta during storm conditions as in Orescanin et al. (2014).

The time-series of $u_{orb,sw}$ and $u_{orb,ig}$ increases during flood as the propagation of SW and IGW is fostered by the rising tide (Fig. 8d and e).
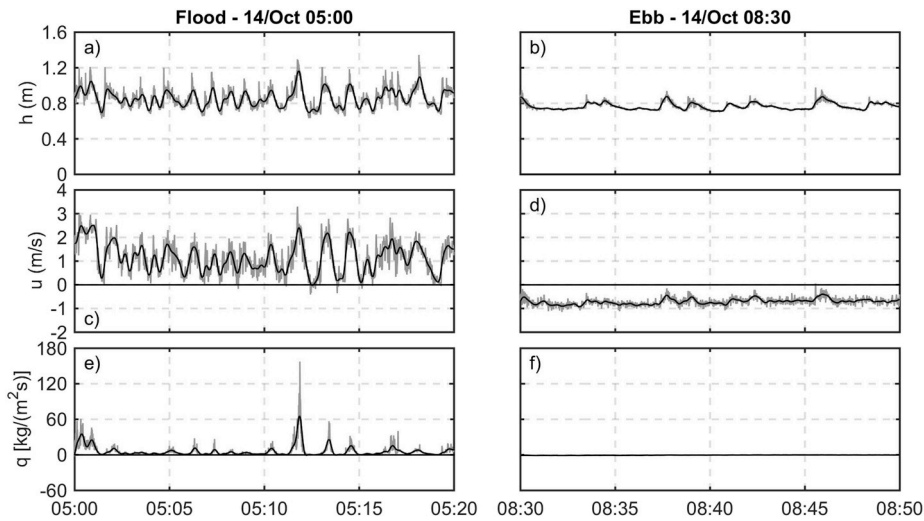
Fig. 9. Raw time-series (grey lines) during flood (left column) and during ebb (right column) of: (a,b) water depth (h); (c,d) horizontal velocity (u); (e,f) suspended sediment transport rate (q) at the ADP1 location. Black lines indicate infragravity wave motions obtained with a 3rd order Butterworth low-pass filter with a cut-off frequency of 0.04 Hz without phase lag.
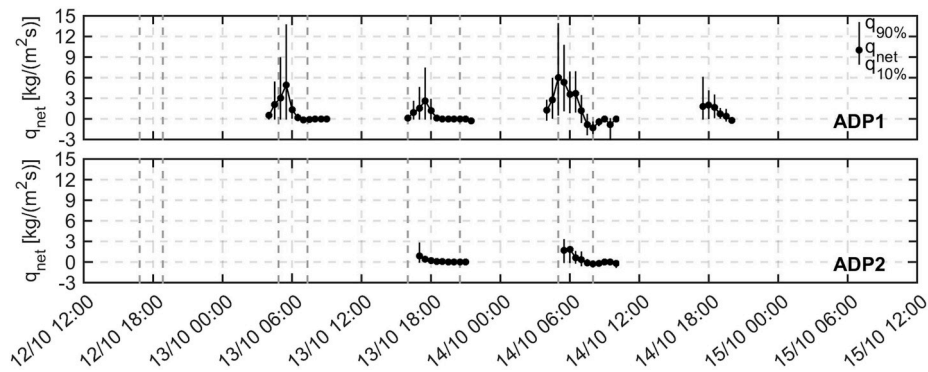

Fig. 10. Time-series of net suspended sediment transport rate (q_{net}, circles) at the ADP1 (top) and at the ADP2 (bottom) locations. Vertical bars indicate the 10% ($q_{10\%}$) and 90% ($q_{90\%}$) quartile values of the suspended sediment transport rate for each block. Vertical dashed lines indicate a similar water depth at flood and ebb at the ADP1 location.

During ebb, $u_{orb,sw}$ and $u_{orb,ig}$ decrease to values close to zero. Moreover, $u_{orb,sw}$ starts to decrease sooner than $u_{orb,ig}$ at the ADP1 and ADP2 locations (Fig. 8d and e). Consequently, $u_{orb,ig}$ can be 2.5 times larger than $u_{orb,sw}$ soon after slack tide at both locations. The previously mentioned temporal variations of $u_{orb,sw}$ and $u_{orb,ig}$ result in general from the interaction with ebb currents. Wave blocking by ebb currents is frequency-dependent (Bertin and Olabarrieta, 2016) and SW frequencies are blocked earlier in time than IGW frequencies. The maximum values of $u_{orb,sw}$ (~0.4 m/s) were approximately constant between October 12–15 at the ADP1 location because SW energy is depth-controlled due to depth-induced breaking at the northern sand spit. In contrast, the maximum values of $u_{orb,ig}$ were largest on October 14 (~0.8 m/s) at the same location. Similar to $H_{m0,ig}$, this indicates that IGW energy depends on the offshore wave conditions, which were the most intense on October 14.

5. Sediment dynamics and morphological changes

The time-series of h, u and q during the most energetic offshore wave conditions (October 14) at maximum flood and ebb illustrate the differences between flood and ebb (Fig. 9, at ADP1). During the flood, large positive values of q were associated with peaks in horizontal velocities with an IGW time scale $O(1 \text{ min})$. These large values of u, associated with IGW crests, are responsible for the instantaneous increase of the q

values by up to two orders of magnitude (Bertin et al., 2019). During the ebb, q values are very close to zero. Therefore, suspended sediment transport is mainly directed landward during flood and is negligible during the ebb at the flood-delta.

The values of q_{net} increased during flood and displayed negligible values during ebb (Fig. 10). In the absence of waves (SW and IGW), which occurs during the ebb due to wave blocking, the values of $q_{10\%}$ and of $q_{90\%}$ are similar to the values of q_{net}. When waves are present, the values of $q_{10\%}$ and of $q_{90\%}$ strongly differ from those of q_{net}. In the latter case, $q_{90\%}$ largely exceeds q_{net}, thereby highlighting the importance of the wave-induced suspended sediment transport. Moreover, the values of q_{net} at the ADP2 location were much smaller than at the ADP1 location (Fig. 10). Even considering that the OBS at the ADP2 location was located 0.05 m above the OBS at ADP1, our results suggest that the suspended sediment transport is more intense at the flood-delta and decreases landward. This decrease is associated with a landward decline of IGW energy between the ADP1 and ADP2 locations (Fig. 7a). The difference between q_{net} at the ADP1 and ADP2 locations is associated with a suspended sediment transport spatial gradient that can promote accretion at the flood-delta.

To further highlight the importance of the wave-induced suspended sediment transport, Fig. 11 depicts the relationship between d, $\overline{u}$ and q_{net}. The magnitude of u_{orb} is shown by the size of the vertical bars. During flood, positive values of $\overline{u}$ are associated with positive and large
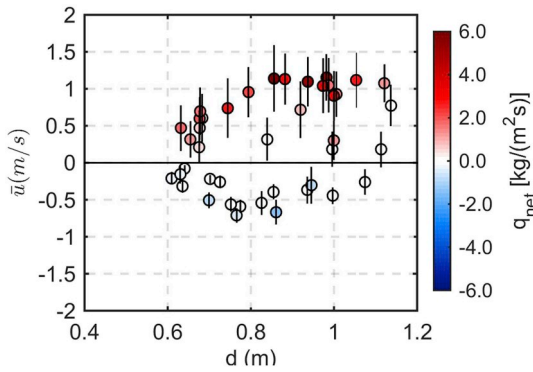
Fig. 11. Scatter diagram of the time-averaged water depth (d), time-averaged velocity ($\overline{u}$) and net suspended sediment transport rate (q_{net}) at the ADP1 location. Vertical bars indicate the magnitude of the wave-generated orbital velocity. (For interpretation of the references to colour in this figure legend, the reader is referred to the Web version of this article.)

values of q_{net} and with large values of u_{orb}. During ebb, negative values of $\overline{u}$ are associated with negligible values of q_{net} and small values of u_{orb}. Moreover, the values of q_{net} are much larger during flood than during ebb for similar $\overline{u}$ which occur for $d < 0.7$ m (Fig. 11). Although the magnitude of flood currents was larger than the magnitude of ebb currents at the ADP1 location (flood-dominance), the association between large values of u_{orb} and large values of q_{net} during flood and not during ebb shows that the contribution of waves for the suspended sediment transport rate is much larger than the tidal currents contribution. The main role of tidal currents on the suspended sediment transport is related to the blocking of waves during ebb, which consequently reduces the values of q_{net}.

In order to assess the relative importance of IGW and SW on suspended sediment transport, the oscillatory suspended sediment

transport (q_{osc}) was decomposed into IGW (q_{ig}) and SW (q_{sw}) contributions through the integration of the co-spectrum (Fig. 12). While the values of q_{ig} increased until the time instants associated with maximum $\overline{u}$ values and were negligible during ebb, the values of q_{sw} were always much smaller. The reduction of q_{ig} during ebb is a consequence of wave blocking. The small values of q_{sw} are associated with strong SW dissipation through depth-induced breaking that occurs over the northern sand spit and with SW refraction and diffraction close to the inlet channel. Moreover, the co-spectral analysis shows that the suspended sediment transport associated with IGW is confined to $f < 0.02$ Hz and is reduced for all IGW frequencies at approximately the same time instant (Fig. 12c). This suggests that the frequency-dependent effect associated with wave blocking by ebb currents is less pronounced for q than for S_η (compare Figs. 4f–12c).

The Leslie storm induced important morphological changes in the Albufeira Lagoon inlet (Fig. 13). At the northern sand spit, the morphological changes that occurred between October 12 and 13 and between October 14 and 15 were modest (<1 m). In contrast, the sediment accumulation reached up to 1.5 m between October 13 and 14, during the most energetic offshore wave conditions (Fig. 13b). This accumulation was responsible for the disconnection between the northern channel and the inlet transitional channel at the flood-delta (Figs. 3–13d).

The OBS measurements at both ADPs are only characteristic of a specific horizontal and vertical location. Still, the major morphological changes (Fig. 13b) are associated with the largest net suspended sediment transport rates at ADP1 (Fig. 10a). This observation suggests that, in this case, the OBS measurements at ADP1 can be representative of the morphological changes that occur at the flood-delta during the most energetic offshore wave conditions.

This large sediment accumulation at the flood-delta was primarily attributed to IGW. The values of $H_{m0,ig}$ increased with more energetic offshore wave conditions (Figs. 4 and 2). Similarly to $H_{m0,ig}$, the values of $u_{orb,ig}$ at the ADP1 location were the largest during the storm (Fig. 8d).
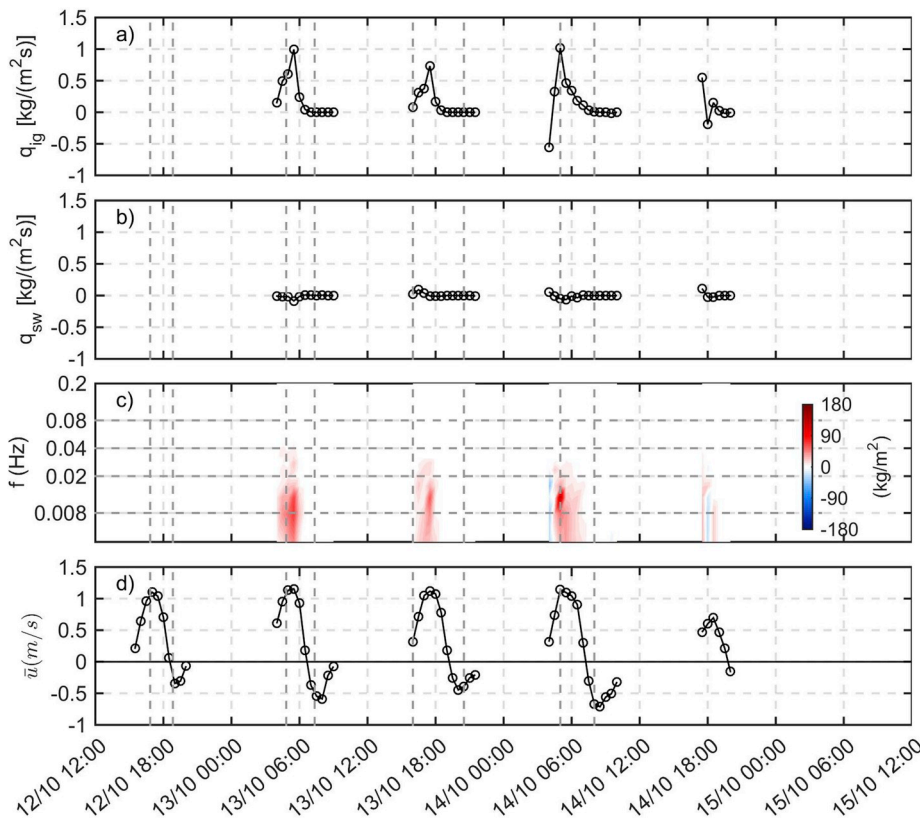

Fig. 12. Time-series of: (a) infragravity component of the oscillatory suspended sediment transport rate (q_{ig}); (b) short-wave component of the oscillatory suspended sediment transport rate (q_{sw}); (c) real part of the co-spectrum between de-trended horizontal velocity and de-trended sediment concentration; (d) the time-averaged velocity ($\overline{u}$) at the ADP1 location. Vertical dashed lines indicate a similar water depth at flood and ebb at the ADP1 location. (For interpretation of the references to colour in this figure legend, the reader is referred to the Web version of this article.)
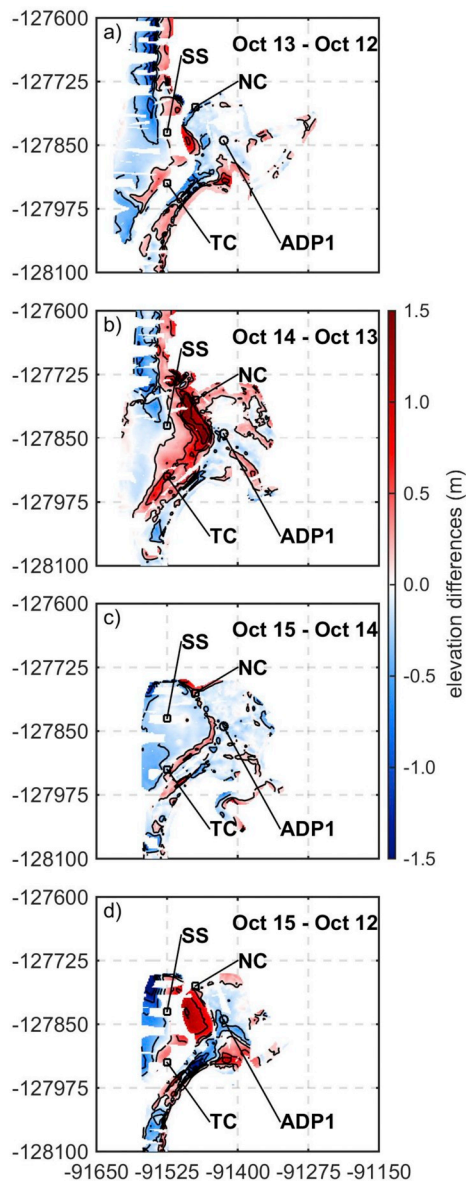
Fig. 13. Differences between the digital elevation models (DEM) obtained with the topographic surveys performed on 12–15 October 2018. The horizontal coordinates are referred in the ETRS89 PT-TM06 system. Blank areas constitute nodes of the DEM grid that have a distance higher than 10 m than any RTK-DGPS measured point. Positive (negative) values indicate accretion (erosion). The annotations stand for NC – northern channel; SS – northern sand spit; TC – inlet transitional channel. (For interpretation of the references to colour in this figure legend, the reader is referred to the Web version of this article.)

The magnitude of tidal currents increased during the storm (Fig. 8) but their contribution to the suspended sediment transport was very small (Fig. 9e and f). Also, because SW inside the lagoon were limited by depth-induced breaking, $u_{orb,sw}$ was unaffected by the storm (Figs. 4b and 8d). Consequently, the short-term morphological changes at the flood-delta induced by storm Leslie are mainly explained by IGW.

The net result of these morphological changes after storm Leslie was a sediment accumulation at the flood-delta and at the transitional channel (Fig. 13d). Moreover, the differences between the topographic surveys before and after the most energetic offshore wave conditions (Fig. 13d) suggest an erosion of the southern margin of the transitional channel with sediment deposited in the lagoon. This sediment accumulation drastically reduced the tidal amplitude inside the lagoon (Fig. 8b) and the cross-sectional area of the transitional channel. The

tidal amplitude reduction decreased the stability of the inlet, eventually leading to inlet's closure which occurred approximately on November 9, 2018 based on satellite images (Bertin et al., 2019).

6. Conclusions

This study investigated the infragravity wave-induced processes and their contribution to the hydro-sedimentary dynamics of a wave-dominated inlet during a storm. We analysed field observations collected at the Albufeira lagoon during the passage of the storm Leslie (2018). These field observations included measurements of hydrodynamics (water levels and horizontal velocities), sediment transport (suspended sediment concentrations) and morphological evolution (topographic surveys).

The physical processes responsible for the variations of IGW energy from the surf zone to the inner lagoon were investigated. At the surf zone, the measured significant IGW height ($H_{m0,ig}$) increased with energetic offshore wave conditions, reaching a maximum of approximately 1 m during storm Leslie. At the seaward limit of the flood-delta, $H_{m0,ig}$ dropped to approximately 0.4 m due to IGW refraction and diffraction near the inlet channel. During flood, currents can reduce $H_{m0,ig}$ by up to 20% and this effect is usually more important in wave-dominated than in tide-dominated inlets due to the higher depths in the latter. During ebb, currents were capable of blocking IGW. The application of a 1D energy flux balance equation over a transect at the flood-delta suggests that the observed reduction of $H_{m0,ig}$ was explained by similar contributions of IGW depth-induced breaking and bottom friction. The analysis of the IGW propagation between the flood-delta and the inner lagoon showed that high-frequency IGW are more easily blocked by ebb currents and are more prone to IGW depth-induced breaking than low-frequency IGW. Consequently, high-frequency IGW are spatially confined to the flood-delta while low-frequency IGW can propagate further into the inner lagoon. Storm Leslie induced a maximum wave setup of 0.30 m on the ocean side of the lagoon. The increase of the mean water level outside due to the wave setup enhanced the tidal range inside the lagoon and the current magnitude observed at the flood-delta. At that location, the calculated IGW orbital velocities were larger than the SW orbital velocities in general, being up to 2.5 times larger soon after slack tide.

Large values of horizontal velocities associated with IGW crests increased the instantaneous suspended sediment transport rate by up to two orders of magnitude during flood at the flood-delta. The net suspended sediment transport rate and its variability associated with the wave motion was positive during flood and negligible during ebb. The positive values were also associated with large wave-induced orbital velocities, suggesting that waves were more important to the suspended sediment transport than tidal currents. The primary role of tidal currents is related to the wave blocking during ebb, which drastically reduces the net suspended sediment transport rate. During flood, the values of the suspended sediment transport rate induced by IGW were much larger than those induced by SW and were directed towards the lagoon. During ebb, these values associated with both IGW and SW were close to zero due to the wave blocking induced by ebb currents. The net suspended sediment transport rate was larger at the flood-delta than near the northern channel. This difference induced a spatial gradient and was associated with sediment accretion near the flood-delta which was responsible for the disconnection between the northern channel and the inlet transitional channel during storm Leslie. Although this sediment accretion did not exclusively result from IGW, these low-frequency waves were shown to play a dominant role in the sedimentary dynamics of wave-dominated inlets during a storm. Future modelling efforts to simulate the morphodynamics of these inlets during storm conditions must therefore take IGW into account.

APPENDIX A. Formulation of the 1D energy flux balance equation

Following Dean and Dalrymple. (1992), the depth-integrated steady-state cross-shore energy flux balance equation neglecting alongshore variations reads:

$$\frac{d}{ds}\left[\frac{1}{8}\rho g H_{rms,ig}{}^2\left(\sqrt{gd}+U_s\right)\right]=-D_f-D_b \tag{A.1}$$

where ρ is the water density, s is the horizontal axis along the transect, $H_{rms,ig}=H_{m0,ig}/(2)^{0.5}$ is the root-mean square IGW height, U_s is the depth-integrated and time-averaged velocity along the transect and D_f and D_b represent the IGW energy dissipation through bottom friction and depth-induced breaking, respectively.

We adopted the bottom friction formulation of Thornton and Guza (1983) in the shallow water regime:

$$D_f=\rho f_w\frac{1}{16\sqrt{\pi}}\left[\frac{H_{rms,ig}}{\sqrt{d/g}}\right]^3 \tag{A.2}$$

where f_w is a friction coefficient. f_w was calculated following Nielsen (2009).

$$f_w=exp\left[5.5\left(\frac{r}{A}\right)^{0.2}-6.3\right] \tag{A.3}$$

where r is the hydraulic roughness, $A=u^{LT}{}_{orb,ig}T_{m02,ig}/(2\pi)$ is the wave orbital excursion and $u^{LT}{}_{orb,ig}=H_{rms,ig}\,(g/d)^{0.5}/2$ is the IGW orbital velocity based on linear wave theory in shallow waters.

The value of r over movable beds is difficult to estimate and constitutes an unsolved issue (e.g. Nielsen, 2009; Trowbridge and Lentz, 2018). Nielsen (2009) estimates r as

$$r=8\frac{\eta_b{}^2}{\lambda}+170\sqrt{\theta_{2.5}-0.05}d_{50} \tag{A.4}$$

where η_b is the bed form height, λ is the bed form wavelength and d_{50} is the median sediment diameter. We set $\eta_b=0.1$ m and $\lambda=1$ m, based on visual observations in the field, and $d_{50}=0.0009$ m based on grain size analysis performed on sediment samples collected in the field near the ADP1, PT5 and PT4 locations. $\theta_{2.5}$ is the nominal grain roughness Shield parameter computed as

$$\theta_{2.5}=\frac{0.5f_{2.5}\left(2\pi A T_{m02,ig}\right)^2}{(s-1)gd} \tag{A.5}$$

where $s=2.65$ is the ratio between the grain and the water density. $f_{2.5}$ is the nominal grain roughness friction factor

$$f_{2.5}=exp\left[5.5\left(\frac{2.5d_{50}}{A}\right)^{0.2}-6.3\right] \tag{A.6}$$

The resulting value of f_w is therefore variable in space and in time which is closer to field conditions than using a constant f_w.

D_b in (A.1) was computed with the formulation given by Thornton and Guza (1983):

$$D_b=\frac{3\sqrt{\pi}}{16}\rho g B^3\frac{1}{T_{02,ig}}\frac{H_{rms,ig}{}^5}{\gamma_{1DEB}{}^2 d^3}\left[1-\frac{1}{\left(1+\left(H_{rms,ig}/\gamma_{1DEB}d\right)^2\right)^{5/2}}\right] \tag{A.7}$$

where $B=1$ and $\gamma_{1DEB}=0.4$ are empirical coefficients associated with wave breaking.

In the sensitivity analysis, r was also computed as

$$r=27.7\frac{\eta_b{}^2}{\lambda}+170\sqrt{\theta_{2.5}-0.05}d_{50}+2.5d_{50} \tag{A.8}$$

(A.4) and (A.8) use the same r contribution due to bed-load sediment transport (second term). The differences between (A.4) and (A.8) are as follows.

The calculation of r induced by ripples (first term) in (A.8) was given by Grant and Madsen (1982). Moreover, (A.8) includes r induced by sand grains (third term). The computation of r using (A.8) reduced slightly the differences between calculations and observations in terms of significant infragravity wave heights. Therefore, r was calculated with (A.8).

A first-order upwind finite difference numerical scheme was used to discretize (A.1) for a given bottom profile and for a given time-series of d, $H_{m0,ig}$, $T_{m02,ig}$ and U_s at the ADP1 location. The numerical discretization of (A.1) gives:

$$H_{i+1} = \left(\frac{H_i^2 (\sqrt{gd_i} + U_{s,i})}{\sqrt{gd_{i+1}} + U_{s,i+1}} - \frac{\Delta s (D_f + D_b)}{\frac{1}{8} \rho g (\sqrt{gd_{i+1}} + U_{s,i+1})} \right)^{1/2} \tag{A.9}$$

where $\Delta s = 0.1$ m is the spatial discretization and the subscript i indicates the location. The variation of U_s along the transect is determined based on mass conservation using known water depths with the value of U_s (equal to $\overline{u}$) at the ADP1 location.

References

Alvarez Fanjul, E., Perez Gomez, B., Carretero, J.C., Rodríguez Sanchez Arevalo, I., 1998. Tide and surge dynamics along the Iberian Atlantic coast. Oceanol. Acta 21, 131–143. https://doi.org/10.1016/S0399-1784(98)80003-0.

APS, 2018. WWW Document. https://www.apseguradores.pt/Portal/Content_Show.as px?ContentId=3429&PageId=1&MicrositeId=1.

Battjes, J.A., Bakkenes, H.J., Janssen, T.T., van Dongeren, A.R., 2004. Shoaling of subharmonic gravity waves. J. Geophys. Res. 109 https://doi.org/10.1029/2003JC001863.

Bertin, X., de Bakker, A., van Dongeren, A., Coco, G., Andre, G., Ardhuin, F., Bonneton, P., Bouchette, F., Castelle, B., Crawford, W.C., Davidson, M., Deen, M., Dodet, G., Guerin, T., Inch, K., Leckler, F., McCall, R., Muller, H., Olabarrieta, M., Roelvink, D., Ruessink, G., Sous, D., Stutzmann, E., Tissier, M., 2018. Infragravity waves: from driving mechanisms to impacts. Earth Sci. Rev. 177, 774–799. https://doi.org/10.1016/j.earscirev.2018.01.002.

Bertin, X., Fortunato, A.B., Oliveira, A., 2009. A modeling-based analysis of processes driving wave-dominated inlets. Cont. Shelf Res. 29, 819–834. https://doi.org/10.1016/j.csr.2008.12.019.

Bertin, X., Mendes, D., Martins, K., Fortunato, A.B., Lavaud, L., 2019. The closure of a shallow inlet promoted by infragravity waves. Geophys. Res. Lett. 46 (12), 6804–6810. https://doi.org/10.1029/2019GL083527.

Bertin, X., Olabarrieta, M., 2016. Relevance of infragravity waves in a wave-dominated inlet. J. Geophys. Res. Ocean. 121, 5418–5435. https://doi.org/10.1002/2015JC011444.

Bruun, P., 1978. Stability of Tidal Inlets - Theory and Engineering, Developments in Geotecnhical Engineering. Elsevier Scientific, Amsterdam.

De Bakker, A.T.M., Brinkkemper, J.A., van der Steen, F., Tissier, M.F.S., Ruessink, B.G., 2016. Cross-shore sand transport by infragravity waves as a function of beach steepness. J. Geophys. Res. Earth Surf. 121, 1786–1799. https://doi.org/10.1002/2016JF003878.

De Bakker, A.T.M., Tissier, M.F.S., Ruessink, B.G., 2014. Shoreline dissipation of infragravity waves. Cont. Shelf Res. 72, 73–82. https://doi.org/10.1016/j.csr.2013.11.013.

Dean, R.G., Dalrymple, R.A., 1992. Water Wave Mechanics for Engineers and Scientists. In: Advanced Series on Ocean Engineering, Vol. 2. World Scientific, p. 353. https://doi10.1142/97898123855121984.

Dodet, G., 2013. Morphodynamic Modelling of a Wave-Dominated Tidal Inlet: the Albufeira Lagoon (PhD Thesis). Université de La Rochelle.

Dodet, G., Bertin, X., Bruneau, N., Fortunato, A.B., Nahon, A., Roland, A., 2013. Wave-current interactions in a wave-dominated tidal inlet. J. Geophys. Res. Ocean. 118, 1587–1605. https://doi.org/10.1002/jgrc.20146.

Dodet, G., Bertin, X., Taborda, R., 2010. Wave climate variability in the North-East Atlantic Ocean over the last six decades. Ocean Model. 31, 120–131. https://doi.org/10.1016/j.ocemod.2009.10.010.

Drusch, M., Del Bello, U., Carlier, S., Colin, O., Fernandez, V., Gascon, F., Hoersch, B., Isola, C., Laberinti, P., Martimort, P., Meygret, A., Spoto, F., Sy, O., Marchese, F., Bargellini, P., 2012. Sentinel-2: ESA's optical high-resolution mission for GMES operational services. Remote Sens. Environ. 120, 25–36. https://doi.org/10.1016/j.rse.2011.11.026.

Fiedler, J.W., Brodie, K.L., McNinch, J.E., Guza, R.T., 2015. Observations of runup and energy flux on a low-slope beach with high-energy, long-period ocean swell. Geophys. Res. Lett. 42, 9933–9941. https://doi.org/10.1002/2015GL066124.

Fortunato, A.B., Freire, P., Bertin, X., Rodrigues, M., Ferreira, J., Liberato, M.L.R., 2017. A numerical study of the February 15, 1941 storm in the Tagus estuary. Continental Shelf Research 144, 50–64. https://doi.org/10.1016/j.csr.2017.06.023.

Fortunato, A.B., Nahon, A., Dodet, G., Rita Pires, A., Conceição Freitas, M., Bruneau, N., Azevedo, A., Bertin, X., Benevides, P., Andrade, C., Oliveira, A., 2014. Morphological evolution of an ephemeral tidal inlet from opening to closure: the Albufeira inlet, Portugal. Cont. Shelf Res. 73, 49–63. https://doi.org/10.1016/j.csr.2013.11.005.

Freitas, M.C., 1995. A Laguna de Albufeira (Península de Setúbal), sedimentologia, morfologia e morfodinàmica (PhD Thesis, in Portuguese). Faculty of Sciences of University of Lisbon.

Grant, W.D., Madsen, O.S., 1982. Movable bed roughness in unsteady oscillatory flow. J. Geophys. Res. 87, 469–481. https://doi.org/10.1029/JC087iC01p00469.

Guedes, R.M.C., Bryan, K.R., Coco, G., 2013. Observations of wave energy fluxes and swash motions on a low-sloping, dissipative beach. J. Geophys. Res. Ocean. 118 (7), 3651–3669. https://doi.org/10.1002/jgrc.20267.

Guérin, T., Bertin, X., Coulombier, T., De Bakker, A.T.M., 2018. Impacts of wave-induced circulation in the surf zone on wave setup. Ocean Model. 123, 86–97. https://doi.org/10.1016/j.ocemod.2018.01.006.

Guerreiro, M., Fortunato, A.B., Freire, P., Rilo, A., Taborda, R., Freitas, M.C., Andrade, C., Silva, T., Rodrigues, M., Bertin, X., Azevedo, A., 2015. Evolution of the hydrodynamics of the Tagus estuary (Portugal) in the 21st century. J. Integr. Coast. Zo. Manag. 15, 65–80. https://doi.org/10.5894/rgci515.

Hayes, M.O., 1979. Barrier island morphology as a function of tidal and wave regime. In: Leatherman, S.P. (Ed.), Barrier Islands Form the Gulf of St. Lawrence to the Gulf of Mexico. New York Academic Press, pp. 1–27.

Holthuijsen, L.H., 2007. Waves in Oceanic and Coastal Waters. Cambridge University Press, p. 387. https://doi.org/10.1017/CBO9780511618536.

Inch, K., Davidson, M., Masselink, G., Russell, P., 2017. Observations of nearshore infragravity wave dynamics under high energy swell and wind-wave conditions. Cont. Shelf Res. 138, 19–31. https://doi.org/10.1016/j.csr.2017.02.010.

Keulegan, G.H., 1967. Tidal Flow in Entrances: Water Level Fluctuations of Basins in Communication with Seas, vol.14. US Army Corps of Engineers, Vicksburg, MS. Tecnhinal Bulletin No.

Martins, K., Blenkinsopp, C.E., Almar, R., Zang, J., 2017. The influence of swash-based reflection on surf zone hydrodynamics: a wave-by-wave approach. Coast. Eng. 122, 27–43. https://doi.org/10.1016/j.coastaleng.2017.01.006.

Martins, K., Blenkinsopp, C.E., Deigaard, R., Power, H.E., 2018. Energy dissipation in the inner surf zone: new insights from LiDAR-based roller geometry measurements. J. Geophys. Res. Ocean. 123 (5), 3386–3407. https://doi.org/10.1029/2017JC013369.

McCall, R.T., Van Thiel de Vries, J.S.M., Plant, N.G., van Dongeren, A.R., Roelvink, J.A., Thompson, D.M., Reniers, A.J.H.M., 2010. Two-dimensional time dependent hurricane overwash and erosion modeling at Santa Rosa Island. Coast. Eng. 57, 668–683. https://doi.org/10.1016/j.coastaleng.2010.02.006.

McSweeney, S.L., Kennedy, D.M., Rutherfurd, I.D., Stout, J.C., 2017. Intermittently closed/open lakes and lagoons: their global distribution and boundary conditions. Geomorphology 292, 142–152.

Mendes, D., Pinto, J.P., Pires-Silva, A.A., Fortunato, A.B., 2018. Infragravity wave energy changes on a dissipative barred beach: a numerical study. Coast. Eng. 140, 136–146. https://doi.org/10.1016/j.coastaleng.2018.07.005.

Moreira, S., Freitas, M.C., Andrade, C., Bertin, X., 2019. Processes controlling morphodynamics of artificially breached barriers. Estuar. Coast Shelf Sci. 225, 1–11. https://doi.org/10.1016/j.ecss.2019.05.013, 106231.

Munk, W.H., 1950. Origin and generation of waves. In: International Conference on Coastal Engineering, pp. 1–4.

Newton, A., Icely, J., Cristina, S., Brito, A., Cardoso, A.C., Colijn, F., Riva, S.D., Gertz, F., Hansen, J.W., Holmer, M., Ivanova, K., Leppäkoski, E., Canu, D.M., Mocenni, C., Mudge, S., Murray, N., Pejrup, M., Razinkovas, A., Reizopoulou, S., Pérez-Ruzafa, A., Schernewski, G., Schubert, H., Carr, L., Solidoro, C., Viaroli, P., Zaldívar, J.M., 2014. An overview of ecological status, vulnerability and future perspectives of European large shallow, semi-enclosed coastal systems, lagoons and transitional waters. Estuar. Coast Shelf Sci. 140, 95–122. https://doi.org/10.1016/j.ecss.2013.05.023.

Nielsen, P., 2009. Coastal and Estuarine Processes. Advanced Series on Ocean Engineering - Volume 29. World Scientific, p. 343.

Olabarrieta, M., Warner, J.C., Kumar, N., 2011. Wave-current interaction in Willapa Bay. J. Geophys. Res. Ocean. 116 (C12), 1–27. https://doi.org/10.1029/2011JC007387.

Oliveira, A., Fortunato, A.B., Rego, J.R.L., 2006. Effect of morphological changes on the hydrodynamics and flushing properties of the Óbidos lagoon (Portugal). Cont. Shelf Res. 26, 917–942. https://doi.org/10.1016/j.csr.2006.02.011.

Orescanin, M.M., Raubenheimer, B., Elgar, S., 2014. Observations of wave effects on inlet circulation. Cont. Shelf Res. 82, 37–42. https://doi.org/10.1016/j.csr.2014.04.010.

Orescanin, M.M., Scooler, J., 2018. Observations of episodic breaching and closure at an ephemeral river. Cont. Shelf Res. 166, 77–82. https://doi.org/10.1016/j.csr.2018.07.003.

Osborne, P.D., Greenwood, B., 1992. Frequency dependent cross-shore suspended sediment transport. 1. A non-barred shoreface. Mar. Geol. 106, 1–24.

Pasch, R.J., Roberts, D.P., 2019. Tropical Cyclone Report: Hurricane Leslie. AL132018.

Penney, W.G., Price, A.T., 1952. Part I. The diffraction theory of sea waves and the shelter afforded by breakwaters. Philos. Trans. R. Soc. A Math. Phys. Eng. Sci. 244, 236–253. https://doi.org/10.1098/rsta.1952.0003.

Power, H.E., Hughes, M.G., Aagaard, T., Baldock, T.E., 2010. Nearshore wave height variation in unsaturated surf. J. Geophys. Res. Ocean. 115, 1–15. https://doi.org/10.1029/2009JC005758.

Quadrio, A., Taborda, R., 2009. Chapter 9 - Portugal-Western coast. In: Ferreira, Ó., Vousdoukas, M., Ciavola, P. (Eds.), Review of Climate Change Impact on Storm Occurrence. Micore Project Deliverable 202798, pp. 71–78.

Rijnsdorp, D.P., Ruessink, G., Zijlema, M., 2015. Infragravity-wave dynamics in a barred coastal region, a numerical study. J. Geophys. Res. Ocean. 120, 4068–4089. https://doi.org/10.1002/2014JC010450.

Roelvink, D., Reniers, A., van Dongeren, A., van Thiel de Vries, J., McCall, R., Lescinski, J., 2009. Modelling storm impacts on beaches, dunes and barrier islands. Coast. Eng. 56, 1133–1152. https://doi.org/10.1016/j.coastaleng.2009.08.006.

Roelvink, J.A., 1993. Dissipation in random wave groups incident on a beach. Coast. Eng. 19 (1–2), 127–150. https://doi.org/10.1016/0378-3839(93)90021-Y.

Ruju, A., Lara, J.L., Losada, I.J., 2012. Radiation stress and low-frequency energy balance within the surf zone: a numerical approach. Coast. Eng. 68, 44–55. https://doi.org/10.1016/j.coastaleng.2012.05.003.

Sheremet, A., Guza, R.T., Elgar, S., Herbers, T.H.C., 2002. Observations of nearshore infragravity waves: seaward and shoreward propagating components. J. Geophys. Res. 107, 1–10. https://doi.org/10.1029/2001JC000970.

Smith, J.M., 2002. Wave pressure gauge analysis with current. J. Waterw. Port, Coast. Ocean Eng. https://doi.org/10.1061/(ASCE)0733-950X(2002)128:6(271).

Speer, P.E., Aubrey, D.G., 1985. A study of non-linear tidal propagation in shallow inlet/estuarine systems Part II: Theory. Estuar. Coast Shelf Sci. https://doi.org/10.1016/0272-7714(85)90097-6.

Storlazzi, C.D., Jaffe, B.E., 2002. Flow and sediment suspension events on the inner shelf of central California. Mar. Geol. 181, 195–213. https://doi.org/10.1016/S0025-3227(01)00267-5.

Thornton, E.B., Guza, R.T., 1983. Transformation of wave height distribution. J. Geophys. Res. 88, 5925–5938. https://doi.org/10.1029/JC088iC10p05925.

Trowbridge, J.H., Lentz, S.J., 2018. The bottom boundary layer. Ann. Rev. Mar. Sci. 10, 397–420. https://doi.org/10.1146/annurev-marine-121916-063351.

Tucker, M.J., 1950. Surf beats: sea waves of 1 to 5 min. Period. Proc. R. Soc. A Math. Phys. Eng. Sci. https://doi.org/10.1098/rspa.1950.0120.

van Dongeren, A., Battjes, J., Janssen, T., van Noorloos, J., Steenhauer, K., Steenbergen, G., Reniers, A., 2007. Shoaling and shoreline dissipation of low-frequency waves. J. Geophys. Res. Ocean. 112 https://doi.org/10.1029/2006JC003701.

Wargula, A., Raubenheimer, B., Elgar, S., 2014. Wave-driven along-channel subtidal flows in a well-mixed ocean inlet. J. Geophys. Res. Ocean. 119, 2987–3001. https://doi.org/10.1002/2014JC009839.

Wargula, A., Raubenheimer, B., Elgar, S., Chen, J.L., Shi, F., Traykovski, P., 2018. Tidal flow asymmetry owing to inertia and waves on an unstratified, shallow ebb shoal. J. Geophys. Res. Ocean. 123, 6779–6799. https://doi.org/10.1029/2017JC013625.

Welch, P.D., 1967. The use of fast fourier transform for the estimation of power spectra: a method based on time averaging over short, modified periodograms. IEEE Trans. Audio Electroacoust. https://doi.org/10.1109/TAU.1967.1161901.

Wiberg, P.L., Sherwood, C.R., 2008. Calculating wave-generated bottom orbital velocities from surface-wave parameters. Comput. Geosci. 34, 1243–1262. https://doi.org/10.1016/j.cageo.2008.02.010.

Williams, M.E., Stacey, M.T., 2016. Tidally discontinuous ocean forcing in bar-built estuaries: the interaction of tides, infragravity motions, and frictional control. J. Geophys. Res. Ocean 121 (1), 571–585. https://doi.org/10.1002/2015JC011166.

Wright, L.D., Guza, R.T., Short, A.D., 1982. Dynamics of a high-energy dissipative surf zone. Mar. Geol. 45, 41–62. https://doi.org/10.1016/0025-3227(82)90179-7.

Wright, L.D., Short, A.D., 1984. Morphodynamic variability of surf zones and beaches: a synthesis. Mar. Geol. 56, 93–118. https://doi.org/10.1016/0025-3227(84)90008-2.